LA-UR-25-29237
Accepted Manuscript

The origin of metallic conductivity in Pt3O4: a first principles study

Peeketi, Akhil Reddy
Rekhi, Lavie
Munoz, Alexander Reed
Jayan, Rahul
Holby, Edward F.
Uberuaga, Blas P.
Jones, Travis Elliott Loyd

To be published in: Electronic Structure

DOI to publisher's version: 10.1088/2516-1075/ae2a8a

Permalink to record:
https://permalink.lanl.gov/object/view?what=info:lanl-repo/lareport/LA-UR-25-29237

Electronic Structure

PURPOSE-LED
PUBLISHING™

PAPER • **OPEN ACCESS**

The origin of metallic conductivity in Pt_3O_4: a first principles study

To cite this article: Akhil R Peeketi *et al* 2026 *Electron. Struct.* **8** 015002

IOP Publishing Electron. Struct. 8 (2026) 015002 https://doi.org/10.1088/2516-1075/ae2a8a

Electronic Structure

RECEIVED
1 October 2025

REVISED
21 November 2025

ACCEPTED FOR PUBLICATION
9 December 2025

PUBLISHED
19 January 2026

PAPER

The origin of metallic conductivity in Pt_3O_4: a first principles study

Akhil R Peeketi[1,*], **Lavie Rekhi**[1], **Alexander R Muñoz**[1], **Rahul Jayan**[1], **Edward F Holby**[1], **Blas P Uberuaga**[2] and **Travis E Jones**[1,*]

[1] Theoretical Division, Los Alamos National Laboratory, Los Alamos, NM 87545, United States of America
[2] Materials Science and Technology Division, Los Alamos National Laboratory, Los Alamos, NM 87545, United States of America
[*] Authors to whom any correspondence should be addressed.

E-mail: peeketiakhilreddy@gmail.com and tejones@lanl.gov

Keywords: density functional theory (DFT), projected density of states (PDOS), electronic conductivity, crystal orbital Hamilton population (COHP), electrocatalysis, platinum oxides, Pt_3O_4

Abstract

The platinum oxide Pt_3O_4 exhibits metallic conductivity even though it contains square-planar PtO_4 units, which in related oxides such as PtO are usually associated with insulating behavior. To identify the electronic origin of this anomalous metallicity, we performed a comprehensive first-principles study using the PBE and r^2SCAN functionals together with Hubbard U corrections and spin-orbit coupling (SOC). Structural benchmarks show that r^2SCAN with SOC and a moderate U value (< 4 eV) reproduces the experimental lattice constants and formation enthalpy, whereas larger U values (~ 8 eV) destabilize the cubic structure. Across all functionals and U values considered in this work, Pt_3O_4 remains metallic. Analyses of the projected density of states, band structures, charge-density isosurfaces, and bonding characteristics demonstrate that the dominant contribution to the metallic character originates from delocalized Pt–O–Pt hybridized antibonding states at the Fermi level. Direct Pt–Pt interactions are present but contribute less strongly to the conductivity. Bader charge analysis reveals only weak Pt charge disproportionation, consistent with mixed Pt^{II}/Pt^{III} character, and a small charge-transfer energy that prevents localization of the Pt $5d$ electrons even at elevated U. In contrast, PtO develops a Mott or charge-transfer gap under modest U despite having the same PtO_4 coordination environment. These findings demonstrate that persistent Pt–O–Pt covalency is the primary driver of metallicity in Pt_3O_4 and support the view that this phase can remain conductive under oxygen reduction and oxygen evolution reaction conditions in fuel cell and electrolyzer environments.

1. Introduction

The oxygen reduction reaction (ORR) is a key electrochemical process in fuel cells through which energy is extracted from hydrogen and oxygen gases. However, ORR is kinetically sluggish, limiting fuel cell performance and necessitating the use of catalysts. Platinum (Pt) is widely considered as the benchmark catalyst for ORR due to its high activity and stability [1–3]. It is also employed in unitized reversible fuel cells (URFCs) [4], which combine a fuel cell and an electrolyzer—responsible for the oxygen evolution reaction (OER) to generate hydrogen—into a single device. Consequently, the catalytic behavior of Pt in ORR has been extensively studied [1, 2, 5, 6]. Thermodynamically, ORR occurs at potentials below 1.23 V versus the reversible hydrogen electrode (RHE). Although Pt is a good catalyst for ORR, it still exhibits an overpotential [1, 7, 8], with practical operation typically occurring at 0.8 V to 0.9 V versus RHE [2, 5, 9]. Surface oxidation of Pt begins around 0.6 V, while bulk oxidation initiates near 1.3 V versus RHE [10–17]. Density functional theory (DFT) calculations further suggest that bulk oxides such as Pt_3O_4 and PtO_2 may form at even lower potentials, around 0.65 V and 0.75 V, respectively (in accordance with the Materials Project database [18, 19]). Oxidation is more severe in URFCs, where potentials exceed 1.23 V during OER operation, leading to repeated and prolonged exposure of Pt to oxidizing environments. Such conditions can promote irreversible conversion of metallic Pt to surface or bulk oxides [10, 14, 16, 17]. The possibility of platinum surface corrosion during ORR, OER and cycling between them has important technical and scientific consequences for fuel cells and URFCs, as metallic platinum is an effective catalyst, whereas its bulk oxides, such as PtO and PtO_2, are typically semi-conducting and exhibit poor ORR performance [9].

Platinum oxide surfaces resembling Pt_3O_4 and α-PtO_2 are observed upon exposure to electrochemically oxidizing potentials. In particular, Pt_3O_4 has been reported to form on Pt nanoparticles supported on substrates [20–22]—a typical design for catalysts in fuel cells and URFCs [5, 23, 24]—under mildly oxidizing conditions. Furthermore, Pt_3O_4 could form during cycling voltages and sustain through ORR-relevant potentials in fuel cells and URFCs. While PtO and PtO_2 are semiconducting in nature [25–28] and are ineffective for ORR, Pt_3O_4 exhibits metallic conductivity [29, 30], making it a plausible active phase. Recent experimental and theoretical work has explicitly linked changes in Pt–O bonding and the Pt 5*d* electronic structure to ORR and OER kinetics, highlighting the importance of oxidized Pt environments and their electronic structure in determining activity and stability [5, 6, 9].

Interestingly, both PtO and Pt_3O_4 contain PtO_4 motifs, yet the former is semiconducting while the latter is suggested to be metallic [29]. This contrast raises fundamental questions about the underlying electronic structure and bonding. Additionally, the non-integer oxidation state of Pt in Pt_3O_4 (+8/3) suggests the possibility of charge disproportionation, akin to that in Fe_3O_4, where Fe exists in mixed valence states as Fe^{II}/Fe^{III} [31]—an aspect not previously addressed for Pt_3O_4 [29, 30]. Studies on mixed-valence transition metal oxides have shown that the interplay between cation valence, metal–oxygen covalency, and band structure can strongly influence oxygen electrocatalysis [32–34], suggesting that a similar connection may exist for possibly mixed-valence Pt_3O_4. Given its potential presence during ORR, and its unclear electronic properties, it is essential to investigate the atomic and electronic structure of Pt_3O_4. From a technical perspective, understanding the origin of its metallic behavior is critical for the design of Pt-based catalysts if Pt_3O_4 forms and persists in fuel cells and URFCs.

Although the electronic structure of metallic Pt is well captured by standard DFT using the generalized gradient approximation (GGA), a Hubbard U correction is often required to account for localized d-electrons in oxides [29, 35, 36]. While DFT+U has shown success in modeling 3*d* transition metal oxides [37–39], its applicability to 5*d* systems like PtO_x remains unclear. The U in 5*d* systems is typically smaller than their 3*d* counterparts due to greater delocalization of electrons [40], and no consensus exists regarding an optimal value. While U can be determined from first-principles [41–43] or fit to experimental data [35, 37, 44], no single value tends to be universally applicable [37, 38, 45]. Furthermore, U can vary with oxidation state and chemical environment [38, 42], complicating thermodynamic calculations, which typically require a single U [46]. Previous work has used values as high as 7.5 eV for Pt in PtO_2 [35] and Pt-CeO_2 [36], but such values are at the strongly correlated limit and are more appropriate for 3*d* oxides [47]. For Pt-based 5*d* systems, values in the range of 1.5–2 eV are more reasonable [40]. Notably, Pt_3O_4 remains metallic even with high U values [29], suggesting the choice of U primarily affects quantitative results such as formation enthalpies rather than qualitative properties. Meta-GGA functionals such as SCAN and its regularized form, r^2SCAN, [48, 49] offer an alternative to DFT+U, providing improved accuracy in describing transition metal oxides and possibly alleviating the ambiguity associated with U. These functionals have shown promise for 3*d* oxides such as Mn, Fe, Co, and Ni [50, 51]. Additionally, since Pt is a 5*d* element with strong spin-orbit coupling (SOC), including SOC may be necessary to accurately model its structural and electronic properties [52, 53].

To address these questions, we performed DFT calculations on Pt_3O_4 using the Perdew–Burke–Ernzerhof (PBE) GGA and r^2SCAN meta-GGA functionals, both with and without a Hubbard U correction and SOC. This enables us to assess the influence of different computational choices on the structural and electronic properties of Pt_3O_4. We also conducted a Bader charge analysis [54–56] to examine charge disproportionation, and a Bader critical point analysis to identify bonding features. Moreover, we have performed orbital-based calculations [57, 58] to identify the bonding and antibonding contributions for different orbital-pair interactions and gain further insight into the chemical bonding in Pt_3O_4. Through density of states (DOS) and band structure calculations, we elucidate why Pt_3O_4 is metallic whereas PtO is semiconducting. The metallic nature of Pt_3O_4 arises from the combination of Pt–Pt bonding and Pt–O bonding, which places the material in a mixed valence regime with a small charge transfer energy. Consequently, the addition of a Hubbard U correction is not able to open a band gap in Pt_3O_4 even at the strongly correlated limit. By contrast, PtO behaves as a positive charge transfer insulator, and a small Hubbard U correction opens a band-gap.

2. Computational methods

DFT calculations were performed using the Vienna *ab initio* Simulation Package [59] with a plane-wave energy cutoff of 400 eV, which was verified to sufficiently converge the heats of formation of Pt_3O_4.

Increasing the plane-wave energy cutoff to 450 eV altered the heat of formation by less than 0.02 eV per formula unit, confirming the adequacy of the selected cutoff. Projector augmented wave datasets were used to describe electron-ion interactions. The structures were relaxed using the exchange-correlation potentials described by the PBE type of the generalized gradient approximation (GGA) while considering the spin-polarization. The exchange-correlation potentials described by r^2SCAN (regularized-restored strongly constrained and appropriately normed) type of the metaGGA were also used for relaxation. DFT calculations were performed while considering the influence of SOC and the Hubbard U correction on the Pt 5d manifold. In all calculations, the spin states were initialized with a magnetic moment of 4.0 μ_B on each Pt atom and 0.0 μ_B on each O atom. All structures were relaxed separately with and without imposed symmetry.

All DFT calculations were performed using a Γ-centered Monkhorst–Pack $\boldsymbol{k}$-point mesh of $12 \times 12 \times 12$, which was confirmed to be well-converged in terms of calculated total energy of the Pt_3O_4 unit cell. Increasing the $\boldsymbol{k}$-point mesh to $14 \times 14 \times 14$ changed the total energy by less than 0.005 eV per formula unit, confirming the adequacy of the chosen mesh. The same $12 \times 12 \times 12$ $\boldsymbol{k}$-point mesh was consistently applied across all studied systems, including metallic platinum and other platinum oxides. Structural relaxations were carried out using the Methfessel–Paxton smearing scheme of order 1 with a smearing width of 0.05 eV. For each level of theory, namely, the PBE and r^2SCAN functionals, with and without Hubbard U corrections and SOC, the atomic coordinates were relaxed over 3–5 consecutive steps to account for changes in the plane-wave basis set associated with variations in cell volume. The electronic self-consistency was converged to a threshold of 1×10^{-7} eV, while the ionic relaxations were performed until the residual forces on all atoms were below 1×10^{-4} eV Å^{-1}. Subsequently, a single-point self-consistent field (SCF) calculation was performed to obtain converged charge densities. These charge densities were then used to evaluate the electronic structure (density of states and band structure) using the tetrahedron method of smearing. For semiconducting platinum oxides, Gaussian smearing with a width of 0.05 eV was applied during both the relaxation and SCF steps. Bader charge calculations and critical point analyses were performed on the converged charge densities, following the method described in [55, 56]. For each platinum oxide, Bader charges were computed at all levels of theory considered in this work.

We employed LOBSTER version 5.1.1 to compute Crystal Orbital Hamilton Population (COHP) values using the projected augmented wave method [57, 58]. Following structural optimization, a SCF calculation was conducted to obtain the wavefunction with a sufficient number of bands (NBANDS = 100) required for projection onto atomic orbitals in LOBSTER. To investigate Pt–Pt and Pt–O bonding interactions in Pt_3O_4, we plotted COHP values as a function of energy relative to the Fermi level ($E - E_F$). Specific Pt–Pt and Pt–O atomic pairs were defined in the lobsterin input file to compute the corresponding projected COHP values. To gain orbital-level insight into bonding interactions, we also performed orbital-resolved COHP analysis, which allowed us to isolate contributions from particular orbital pairs on each atom. The electronic-structure analyses (density of states, band structures, charge-density isosurfaces, and COHP) were carried out on the relaxed geometries obtained at each corresponding level of theory. For the PBE+U calculations with $U = 8$ eV, the electronic-structure analysis was instead performed using the PBE-relaxed geometry; the motivation for this choice is discussed in the Results and Discussion section.

3. Results and discussion

3.1. Crystal structure and formation enthalpy

In this section, we evaluate various theoretical approaches (PBE, r^2SCAN, +U, and +SOC) to determine the most suitable methodology for modeling Pt_3O_4 by comparing with experimental crystal structures and formation enthalpies.

Pt_3O_4 crystallizes in a symmetric cubic structure belonging to the Pm$\bar{3}$n space group, with a unit cell consisting of six platinum atoms and eight oxygen atoms, as illustrated in figure 1. The initial structure was obtained from the Materials Project [62] and were fully relaxed at different levels of theory, with all degrees of freedom allowed to vary. The lattice constants predicted at various levels of theory (PBE, r^2SCAN, +U, +SOC) are summarized in table 1. Experimentally, the lattice constant of Pt_3O_4 is measured to be 5.585 Å [60]. At the scalar-relativistic PBE and at the fully relativistic PBE+SOC levels, DFT slightly overestimates the lattice constant relative to experiment. The inclusion of SOC at both the PBE and r^2SCAN levels changes the lattice constant by less than 1%, indicating that relativistic effects have only a minor influence on the DFT-relaxed lattice parameters. In contrast, the inclusion of a moderate Hubbard U (4 eV) results in an underestimation of the lattice constant. This suggests that an intermediate U value could yield lattice parameters closer to the experiment for both PBE

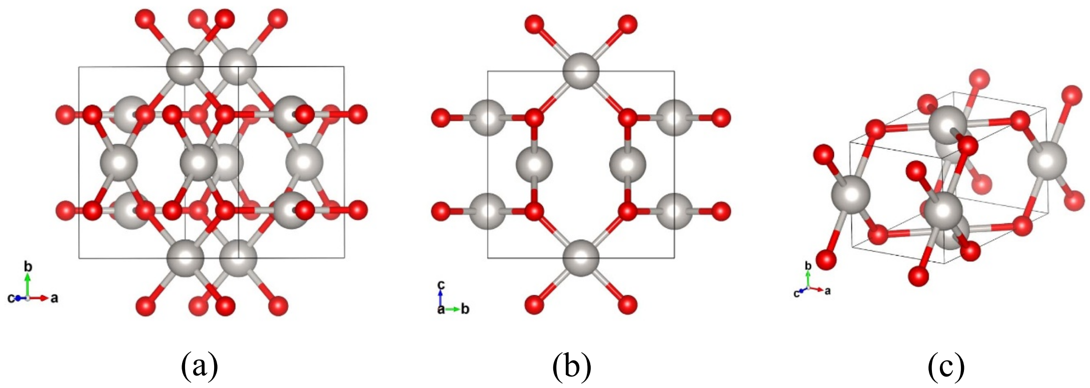

(a) (b) (c)

Figure 1. Crystal structures of (a) and (b) Pt_3O_4 viewed along different crystallographic directions, and (c) PtO, illustrating the presence of PtO_4 units in both compounds. Platinum atoms are represented as gray spheres and oxygen atoms as red spheres.

Table 1. Crystal lattice parameters and formation enthalpies of Pt_3O_4 obtained from DFT calculations using different levels of theory. The lattice angle is consistently found to be 90° in all cases.

Theory	a (Å)	b (Å)	c (Å)	ΔH_f (eV/Pt atom)
PBE	5.609			−1.1
PBE+U(4 eV)	5.564			−1.3
PBE+U(8 eV)	5.678	5.468	5.414	−1.4
PBE+SOC	5.616			−1.1
PBE+SOC+U(4 eV)	5.572			−1.3
PBE+SOC+U(8 eV)	5.732	5.435	5.435	−1.4
r^2SCAN	5.575			−1.3
r^2SCAN+U(4 eV)	5.516			−1.6
r^2SCAN+U(8 eV)	5.654	5.428	5.427	−1.6
r^2SCAN+SOC	5.580			−1.4
r^2SCAN+SOC+U(4 eV)	5.538			−1.5
r^2SCAN+SOC+U(8 eV)	5.653	5.443	5.443	−1.6
Exp	5.585 [60]			−1.69 [61]

and PBE+SOC. Calculations using r^2SCAN and r^2SCAN+U tend to underestimate the unit cell dimensions even further, consistent with the known tendencies of these functionals [63]. Among all tested methods, r^2SCAN+SOC yields a lattice constant of 5.580 Å in the closest agreement with the experimental value. Using a high value of U (8 eV) leads to a symmetry-breaking distortion for both PBE+U and r^2SCAN+U, regardless of the inclusion of SOC. However, experimental data indicates that Pt_3O_4 retains a symmetric structure, indicating that such high values of U are not appropriate, despite the use of similar values (7.5 eV) in previous studies on platinum oxides [35, 36]. The moderate U values that yield agreement with experimental lattice constants are also more consistent with the expectations that U should be low ($<$4 eV) for 5d transition metal oxides. For completeness, we also report representative bond lengths in the relaxed Pt_3O_4 structure. At the r^2SCAN+SOC+U(4 eV) level, the Pt–O distance within the square-planar PtO_4 units is 1.96 Å, and the shortest Pt–Pt separation is 2.77 Å.

In addition to crystal structure, the formation enthalpy is another key experimentally accessible property that can be used to tune the choice of U value [37, 64]. The formation enthalpy (eV) for Pt_3O_4 per Pt atom can be estimated from DFT calculations as,

$$\Delta H_f(\mathrm{Pt_3O_4}) = \frac{1}{3} \times \left(E^{\mathrm{DFT}}_{\mathrm{P_3O_4}} - 3 \times E^{\mathrm{DFT}}_{\mathrm{Pt}} - 4 \times E_{\frac{1}{2}\mathrm{O_2}} \right), \tag{1}$$

where the DFT-calculated energy of $\frac{1}{2}O_2$ is corrected to mitigate the known overbinding of O_2 at the GGA level [65], using the experimental enthalpy of formation of water,

$$E_{\frac{1}{2}\mathrm{O_2}} = E^{\mathrm{DFT}}_{\mathrm{H_2O}} - E^{\mathrm{DFT}}_{\mathrm{H_2}} - \Delta H_f(\mathrm{H_2O}). \tag{2}$$

Here, the experimental enthalpy of formation of gas-phase water is taken as −2.48 eV at 0 K [66]. The formation enthalpies obtained from different levels of theory are compiled in table 1. PBE and PBE+U (with or without SOC) predict formation enthalpies that are less exothermic than the experiment (−1.69 eV/Pt atom) [61]. Within PBE+U, the formation enthalpy becomes more negative with increasing U. r^2SCAN yields more exothermic formation enthalpies than PBE. The cases of r^2SCAN+U ($U > 4$ eV) with or without SOC predict the formation enthalpies closest to the experimental measurement [61]. The inclusion of SOC at both the PBE and r^2SCAN levels changes the predicted formation enthalpies by less than 0.1 eV per Pt atom. Taking into account both the predicted lattice constants and formation enthalpies, r^2SCAN+SOC with a moderate U of 4 eV appears to offer the most accurate description of Pt_3O_4.

3.2. Charge disproportionation

The non-integer formal oxidation state of platinum in Pt_3O_4 suggests the possibility of charge disproportionation. In Pt_3O_4, each Pt occupies an identical local environment, coordinated by four oxygen atoms in a square-planar PtO_4 motif, analogous to that in PtO (see figure 1(c)). In PtO, this geometry is consistent with a formal oxidation state of Pt(II). However, in Pt_3O_4, the structural equivalence implies a formal oxidation state of +2.67 for each Pt atom. Achieving integer formal oxidation states would therefore require charge-disproportionation—either into a one Pt^{IV} and two Pt^{II}, or two Pt^{III} and one Pt^{II}. While such disproportionation has been proposed for Pt_3O_4 [20], it would necessarily break the symmetry of the Pt sites and is typically accompanied by lattice distortions [67–69].

To drive such structural distortions and probe the possibility of charge disproportionation, Pt_3O_4 was initialized with three different geometries: (i) a cubic symmetric structure, (ii) a cubic structure with oxygen atoms distorted around one Pt center, and (iii) a cubic structure with oxygen atoms distorted around three Pt centers. These initial configurations were fully relaxed at different levels of theory, with all degrees of freedom allowed to relax, and only the minimum-energy structures were retained for further analysis. We then performed Bader charge analysis [55] on the relaxed structures to assess charge-disproportionation. The symmetric structure retained identical Bader charges for all Pt atoms. Interestingly, even in cases where the structures initially deviated from symmetry, the relaxation process returned them to nearly symmetric geometries with only minor residual distortions. Notably, these small distortions are still accompanied by a charge disproportionation with a magnitude of 0.18 e. For comparison, in the well-known mixed-valent system Fe_3O_4, the charge separation between Fe^{II} and Fe^{III} is estimated to be 0.18–0.24 e [31]. This suggests that Pt ions in Pt_3O_4 may similarly exist in a weakly disproportionated state, most plausibly as a mixture of Pt^{II} and Pt^{III}, even in the absence of strong structural distortions.

Although Bader charges do not directly yield formal oxidation states, they can often be correlated with formal oxidation states of known reference compounds and then used to assign oxidation states in an unknown phase. To establish such a correlation, we computed the Bader charges of Pt ions in platinum metal, PtO, α-PtO_2, and β-PtO_2 at each level of theory and related them to their formal oxidation states, Pt^0, Pt^{II}, and Pt^{IV} (for both α-PtO_2 and β-PtO_2). We then compared the Pt Bader charges in Pt_3O_4 with these reference values and used the resulting correlation between charge and oxidation state to estimate the oxidation states of Pt in Pt_3O_4. The symmetric Pt_3O_4 structure relaxed at the PBE level yields a Bader-derived oxidation state of approximately +2.9 as seen in figure 2(a). While this deviates slightly from the expected value of +2.67 (based on all oxygen atoms as O^{2-}), the discrepancy may stem from the fitting approach.

DFT calculations with various levels of theory and distorted initial configurations support the existence of modest charge disproportionation in Pt_3O_4 (figure 2(b)). At the PBE level, Pt oxidation states are found to be +2.7 to +3.2, despite the final relaxed structure remaining nearly symmetric. This suggests that only minimal structural distortions are required to induce charge separation. Moreover, the energy of the charge-disproportionate system is nearly identical to that of the non-disproportionated system. Including Hubbard U corrections (PBE+U) up to 6 eV slightly enhances the charge disproportionation. At the PBE+U level with $U = 8$ eV, Bader charge analysis yields oxidation states of approximately +2.5 and +3.1 for Pt, accompanied by a symmetry-breaking distortion of the crystal structure from cubic to orthorhombic (see table 1). The inclusion of SOC at the PBE level leads to charge disproportionation regardless of the initial structure, although the extent remains unchanged with SOC. DFT calculations with r^2SCAN resemble those of PBE. The most pronounced charge disproportionation—oxidation states of +2.5, +3.0, and +3.4 – is observed with r^2SCAN+SOC+U at $U = 8$ eV, although again accompanied by significant structural distortion from cubic to tetragonal. Given that the undistorted structure yields a Bader-derived oxidation state of +2.9 rather than +2.67, the states of +2.5 and +3.4 are assumed to be more consistent with Pt^{II} and Pt^{III} rather than Pt^{II} and Pt^{IV}. However, a U value

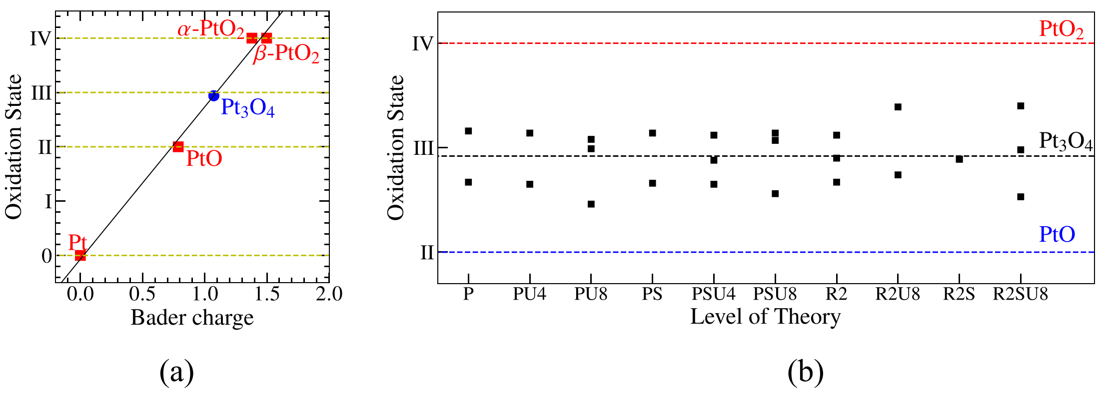

Figure 2. (a) Calibration curve correlating formal oxidation states with Bader charges at the PBE level of theory. (b) Disproportionate oxidation states of Pt ions in Pt_3O_4 as determined from Bader charge analysis using different levels of theory [P—PBE, S—SOC, R2 - r^2SCAN, U4 - U of 4 eV, U8 - U of 8 eV].

of 8 eV leads to pronounced distortion in crystal structure inconsistent with the experimental XRD data for Pt_3O_4 [60]. Therefore, based on our analysis, Pt_3O_4 exhibits only weak charge separation. If a strong charge-disproportionation occurs, it is more likely to involve Pt^{II}/Pt^{III} rather than Pt^{II}/Pt^{IV}—as previously proposed by [20]. Since distorted crystal structures are inconsistent with experimental observations [60] and only appear at high U values (∼8 eV), we restricted our study to the cubic symmetric structures for all further calculations and analyses.

3.3. Electronic structure and metallicity

Figure 3 shows the PDOS for the square-planar PtO_4 motif in Pt_3O_4, calculated at the PBE level of theory, reveals distinct bonding characteristics arising from the orbital interactions between Pt 5d and O 2p orbitals, illustrated by the charge density iso-surfaces shown in the insets. At the PBE level, the spin states are found to be symmetric. The PDOS and the iso-surface corresponding to -6 to -8.5 eV below the Fermi level indicates the strong overlap between the Pt 5 $d_{x^2-y^2}$ orbitals and the O 2p orbitals, forming a σ bond (see inset i of figure 3). The corresponding σ antibonding states are located from 2 to 5 eV above the Fermi level. The large energy separation (≈12 eV) between the σ-bonding and σ-antibonding states underscores the strength of Pt–O hybridization, driven by significant overlap between diffuse Pt 5d and O 2p orbitals, resulting in a highly covalent σ bond. The d_{xy}, d_{yz} and d_{zx} overlap with O 2p contribute to π bonds (see inset iii of figure 3), but the bonding and antibonding states of the π-bond are not easily extractable from the PDOS. In contrast, the d_{z^2}-orbitals of Pt show negligible hybridization with O 2p orbitals but display inter-motif overlap with d_{z^2} orbitals of neighboring PtO_4 units forming a Pt–Pt σ bond at around -5 eV below the Fermi energy (see inset ii of figure 3). Even for these Pt–Pt σ-bonds, the bonding and antibonding states are not clearly identifiable from the PDOS. The presence of finite DOS at the Fermi level confirms the metallic nature of Pt_3O_4, consistent with previous studies [29]. Notably, both Pt 5d and O 2p states contribute at the Fermi level, indicating that metallic conduction arises from a combination of Pt–Pt and Pt–O interactions. To further elucidate the origin of this metallicity, we examined the band structure, PDOS, charge density isosurfaces, and orbital-resolved bonding features across multiple levels of theory.

The band structure and the corresponding total DOS of Pt 5d and O 2p per Pt_3O_4 formula unit calculated at PBE level of theory are shown in figure 4(a), and the coloring indicates the amount of O 2p character as defined by the figure legend. Between -6 eV to -9 eV below the Fermi level, strong hybridization is evident, with nearly equal contributions from Pt 5d and O 2p states, in agreement with the inferences from figure 3. Pure O 2p bands are almost entirely absent, indicating that nearly all O 2p orbitals are engaged in bonding. Pure Pt 5d bands appear around -2.8 eV, while the center of the occupied Pt 5d bands lies near -3.8 eV. Hybridized states with an almost equal contribution from Pt and O dominate the region from -1 eV up to the Fermi level. At the PBE level of theory, two types of bands cross the Fermi level: those predominantly Pt 5d in character and hybridized bands with nearly equal O 2p and Pt 5d character. The charge density iso-surfaces for these bands at the Fermi level (±0.01 eV) shown in figure 4(b) confirm distinct Pt–Pt and Pt–O–Pt bonding contributions. The charge density iso-surface of the Pt-dominated bands shown in figure 4(b)(i) and (ii) indicates that the charge density magnitude of Pt–Pt connectivity (via d_{z^2} overlap) is five times more pronounced than the Pt–O–Pt connectivity (via the overlap of d_{zx}, d_{yz}, d_{xy} with p). The charge density iso-surface of the hybridized Pt

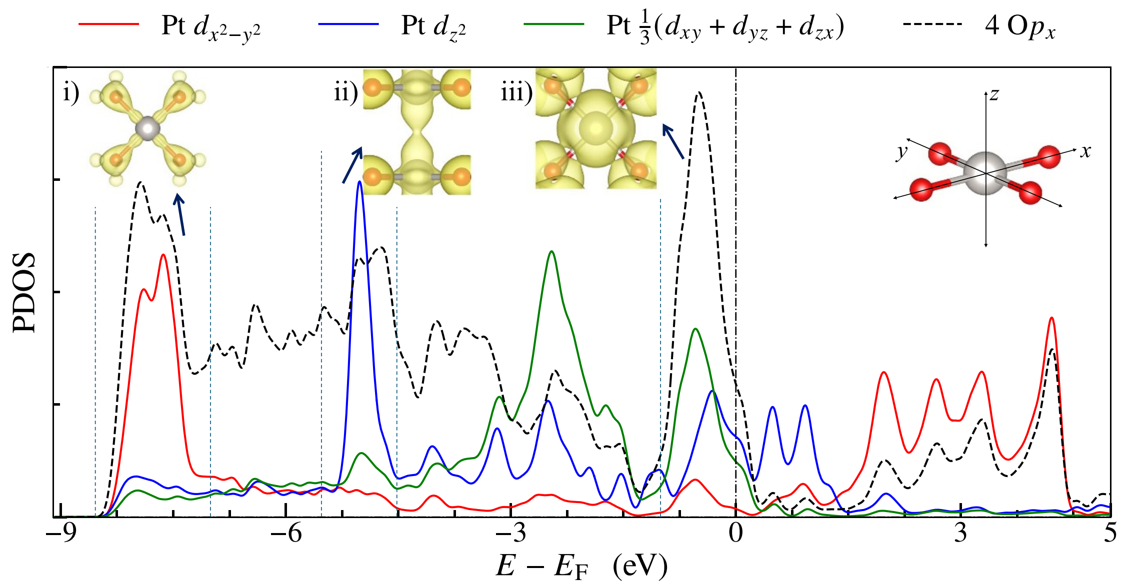

Figure 3. Projected density of states (PDOS) for the Pt 5*d* and O 2*p*-orbitals of the square-planar PtO_4 unit in Pt_3O_4, calculated at the PBE level of theory. The Fermi level, defined as the highest occupied state, is set to 0 eV. The spin channels are found to be symmetric. Insets to the left of the Fermi show the charge-density iso-surfaces spread across specific energy levels marked by dashed vertical lines, highlighting distinct bonding features. The inset to the right of Fermi illustrates the coordinate system used for orbital projection: the *x*- and *y*-axes lie along Pt–O bonds, while the *z*-axis is oriented perpendicular to the PtO_4 plane.

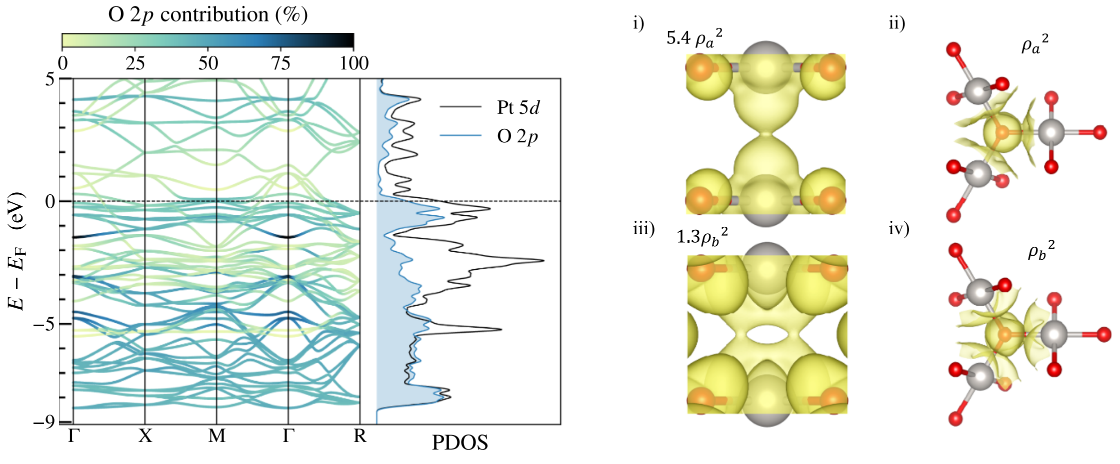

(a) (b)

Figure 4. (a) Electronic band structure and projected density of states for Pt and O atoms in Pt_3O_4, calculated using PBE. The band colors represent the percentage contribution from O 2*p* orbitals. The horizontal dashed line indicates the Fermi energy, set to 0 eV. In the DOS, the Pt 5*d* contribution is shown as a black line and O 2*p* is represented as the blue shaded area. (b) Charge-density iso-surfaces at the Fermi level (±0.01 eV) corresponding to (i) and (ii) Pt-dominated bands and (iii) and (iv) Pt–O hybridized bands. The panels are shown at different isosurface levels to illustrate Pt–Pt and Pt–O–Pt bonding connectivity. Panels (i) and (iii) are viewed along the [100] direction, and panels (ii) and (iv) are viewed along the [111] direction. The specific isosurface values are indicated above each subpanel. The parameters ρ_a^2 and ρ_B^2 are chosen arbitrarily and are used only to facilitate comparison of the charge densities between panels (i) and (ii) and between panels (iii) and (iv), respectively.

and O bands shown in figure 4(b)(iii) and (iv) displays a comparable charge density magnitude for both Pt–Pt and Pt–O–Pt connectivity. The Pt–Pt connection in figure 4(b)(iii) stems from the overlap of the neighboring Pt d_{xy} orbitals, that are strongly hybridized with O p_x. Together, the band structure, and the real-space charge density iso-surfaces highlight the dual role of Pt–Pt and Pt–O bonds in driving metallic conductivity in Pt_3O_4.

To further dissect these interactions, we employed COHP analysis, a method that distinguishes between bonding and antibonding contributions based on the constructive or destructive nature of orbital interactions [57, 58, 70]. Unlike the PDOSs, which do not give an unambiguous assignment of bonding character, COHP directly resolves energy contributions from specific orbital-pair interactions. Figures 5(a) and (b) present the projected COHP (pCOHP) values with respect to the Fermi level and

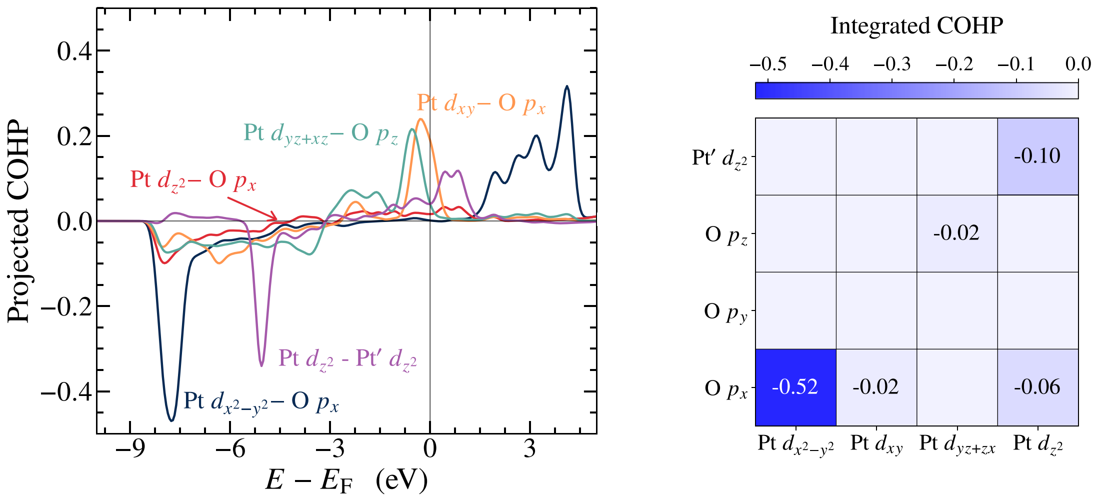

(a) (b)

Figure 5. (a) Projected crystal orbital Hamilton population (pCOHP) curves calculated using PBE for key orbital-pair interactions in Pt_3O_4, with bonding states indicated by negative values (pCOHP < 0) and antibonding states by positive values (pCOHP > 0). The overlap of spin-up (solid lines) and spin-down (dashed lines) interactions indicates spin symmetry. The Fermi energy is set to 0 eV. (b) The integrated COHP (iCOHP) values for the same orbital pairs, providing a quantitative measure of bond strength.

the integrated COHP (iCOHP) values calculated with PBE for key orbital-pair interactions, respectively. Bonding states (pCOHP < 0) dominate between –9 eV and –3 eV, while antibonding states (pCOHP > 0) appear from –3 eV. A particularly strong σ-bond is observed between the Pt $d_{x^2-y^2}$ and O p_x orbitals, as evidenced by the high value for iCOHP. In contrast, σ-bonding between Pt d_{z^2} orbitals of neighboring PtO_4 motifs is significantly weaker. Other orbital interactions mainly involve weak π-bonding. Several antibonding states—Pt d_{xy}–O p_x, Pt d_{z^2}–O p_x, Pt d_{yz+xz}–O p_z, and Pt d_{z^2}–Pt′ d_{z^2}—persist at the Fermi level (figure 5(a)). These findings corroborate the PDOS and charge-density results, confirming that the metallic nature of Pt_3O_4 arises from antibonding states involving both Pt–Pt and Pt–O orbital overlaps. Additionally, COHP analysis confirms that the d_{xy} connection at the Fermi level seen in figure 4(b)(iii) is due to Pt d_{xy}—O p_x hybridization, not direct Pt d_{xy}—Pt′ d_{xy} bonding.

To evaluate the role of the O 2p states in the metallic conductivity of Pt_3O_4 further, we analyzed the influence of onsite Coulumbic interactions on the Pt 5d manifold through the inclusion of a Hubbard U on Pt. We performed the electronic structure calculations on the relaxed cubic symmetric structures obtained at each specific U value, except for $U = 8$ eV. At this high U, the crystal structure distorts from cubic symmetry. Since the experimentally observed phase is cubic [60] and to avoid artifacts from unphysical distortions, the PBE-relaxed cubic structure was used for the PBE+U (8 eV) electronic structure calculations. As shown in figure 6, increasing U enhances the localization of 5d orbitals and shifts the occupied states to lower energies while preserving their hybridization with the O 2p states near the Fermi level. For $U > 4$ eV, the region from -1 eV to the Fermi level becomes increasingly O 2p dominated. At $U = 8$ eV, the O 2p states contribute significantly more than Pt 5d at the Fermi level. The charge density iso-surfaces at $U = 8$ eV (figure 7) show dominant Pt–O–Pt connections with diminished Pt–Pt character. The COHP analysis supports this, with the antibonding states of Pt d_{xy}–O p_x maintaining a significant presence at the Fermi level, see figure 8. A similar trend is observed with the r^2SCAN functional with U, confirming that the Pt–O hybridization underpins the metallic character of Pt_3O_4 even under strong electronic correlations. Moreover, for calculations with PBE with $U = 4$ and 8 eV, the spin channels become asymmetric, as shown in figure 8, leading to slight magnetization with a net magnetic moment of 0.4 μ_B and 1.7 μ_B per formula unit for $U = 4$ and 8 eV, respectively.

Given the presence of heavy Pt atoms, SOC effects must be considered. At the PBE level, inclusion of SOC causes only small changes in the relaxed structure (table 1), but lifts several band degeneracies near the Fermi level, as evident from the comparison between band structures computed with and without SOC (figures 4(a) and 9(b)). We have also computed the band structure at the PBE+SOC+U(4 eV) level (figure 9(b)), which shows that several bands with mixed Pt 5d and O 2p character continue to cross the Fermi level and that the total DOS at E_F remains very similar to the PBE and PBE+U cases. SOC does not induce symmetry breaking in the crystal structure, nor does it open a gap or shift the O

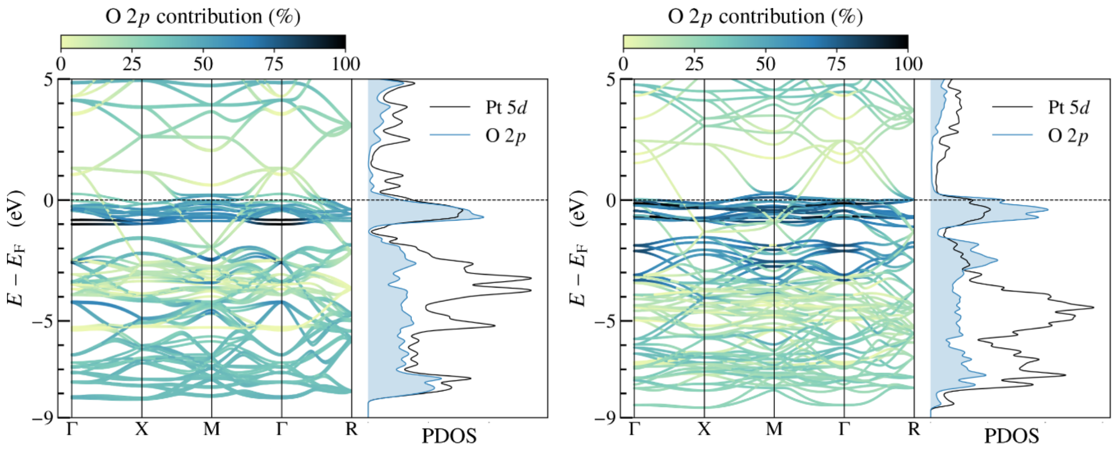

(a) (b)

Figure 6. Electronic band structure and projected total density of states for Pt and O atoms in Pt_3O_4, calculated using PBE+U with U of (a) 4 eV and (b) 8 eV. The band colors represent the percentage contribution from O 2p orbitals. The horizontal dashed line indicates the Fermi energy, set to 0 eV. In the DOS, the Pt 5d contribution is shown as a black line and O 2p is represented as the blue shaded area.

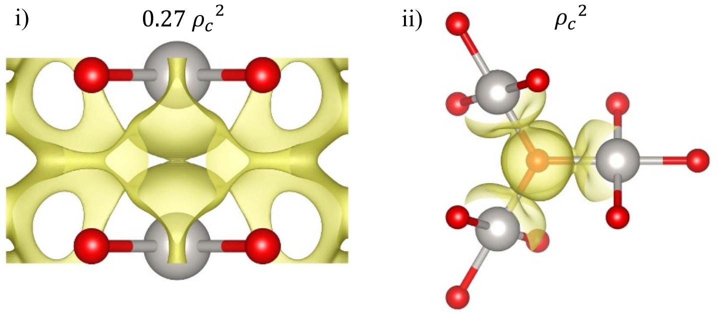

Figure 7. Charge-density iso-surfaces considering all bands at the Fermi level (±0.01 eV) for Pt_3O_4 calculated with PBE+U (8 eV). Panels (i) and (ii) are shown at different isosurface levels to highlight Pt–Pt connectivity (view along the [100] direction) and Pt–O–Pt connectivity (view along the [111] direction), respectively. The specific isosurface values are indicated above each subpanel. The parameter ρ_c^2 is chosen arbitrarily and is used only to facilitate comparison of the charge densities in panels (i) and (ii).

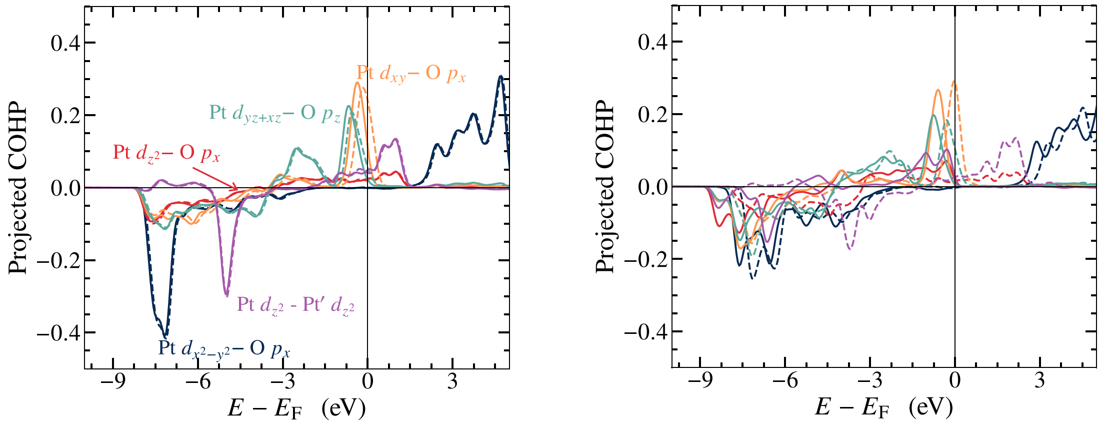

(a) (b)

Figure 8. Projected COHP curves for key orbital-pair interactions in Pt_3O_4 calculated with PBE+U with (a) U of 4 eV and (b) U of 8 eV. The bonding states are indicated by negative values (COHP < 0) and antibonding states by positive values (COHP > 0). The spin up interactions are represented as solid lines, and the spin down by dashed lines. The Fermi energy is set to 0 eV.

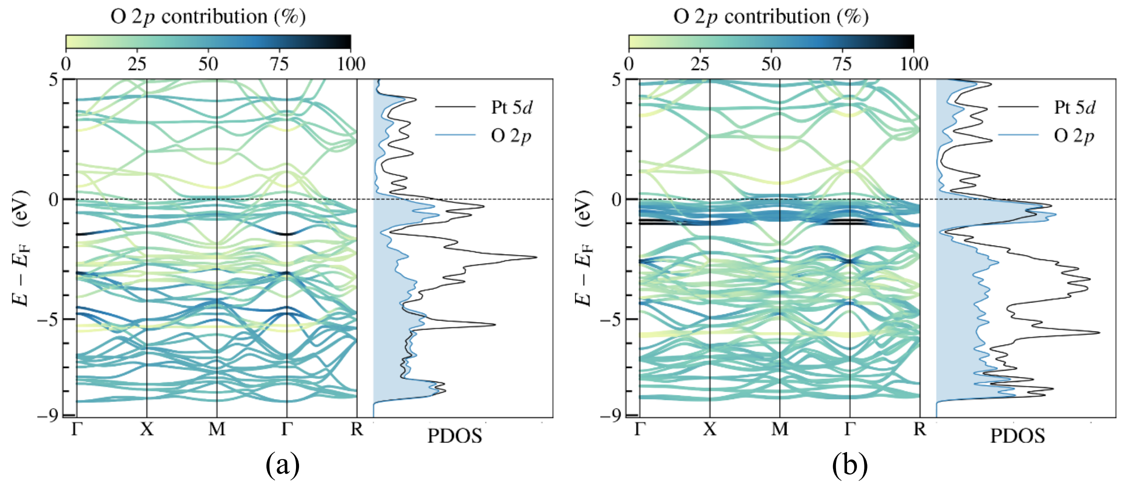

(a) (b)

Figure 9. Electronic band structure and projected density of states for Pt and O atoms in Pt_3O_4, calculated using (a) PBE+SOC and (b) PBE+SOC+U(4 eV). The band colors represent the percentage contribution from O 2p orbitals. The horizontal dashed line indicates the Fermi energy, set to 0 eV. In the DOS, the Pt 5d contribution is shown as a black line and O 2p is represented as the shaded area.

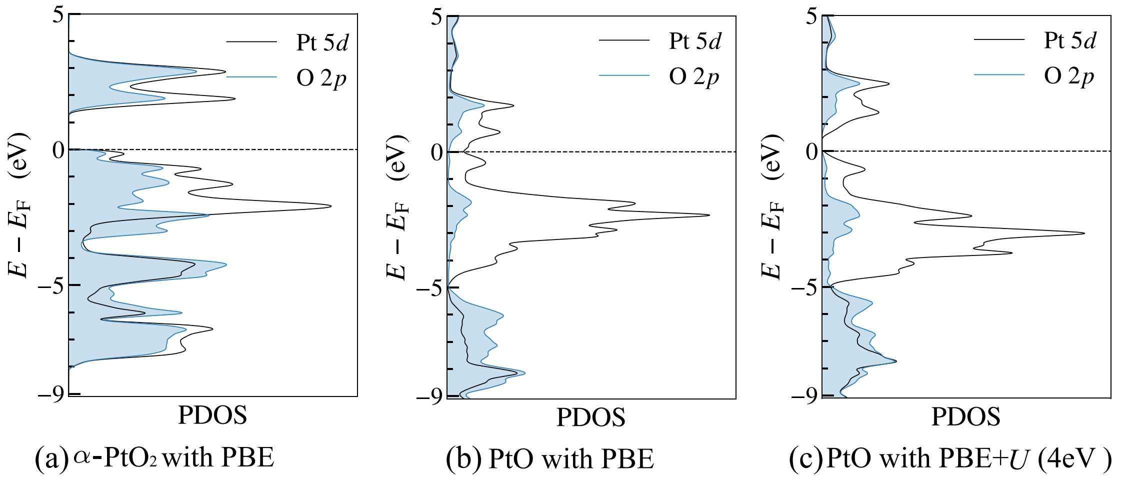

(a) α-PtO_2 with PBE (b) PtO with PBE (c) PtO with PBE+U (4eV)

Figure 10. Projected density of states for Pt and O atoms in (a) α-PtO_2 calculated with PBE, (b) PtO calculated with PBE, and (c) PtO calculated with PBE+U (4 eV). The Pt 5d contribution is shown as a black line and O 2p is represented as the blue shaded area. The black dashed horizontal line indicates the Fermi energy, set to 0 eV.

2p–derived states away from the Fermi level. Taken together with the meta-GGA results, these observations demonstrate that the metallic character of Pt_3O_4 is robust with respect to both SOC and on-site Coulomb interactions. Standard GGA-based calculations, even without SOC, are therefore sufficient to capture the essential features of the electronic structure and metallic nature of Pt_3O_4.

To understand what distinguishes Pt_3O_4 from other Pt oxides, we compared its electronic structure with that of PtO, α-PtO_2, and β-PtO_2. The α and β phases of PtO_2 contain octahedral PtO_6 units, in which the crystal field splits the Pt 5d orbitals into lower-energy t_{2g} and higher-energy e_g levels. In this formal Pt^{IV} (d^6) configuration, the six 5d electrons fully occupy the t_{2g} manifold, leaving the e_g orbitals empty. Strong Pt–O covalency further separates the predominantly O 2p + Pt 5d valence band from the empty e_g-derived conduction band, producing a well-defined d/p–d/p band gap and making these phases semiconducting (see DOS for α-PtO_2 in figure 10(a)). In contrast, both PtO and Pt_3O_4 contain square-planar PtO_4 motifs, where orbital splitting yields a_{1g}, b_{1g}, b_{2g}, and e_g states. PBE calculations incorrectly predict PtO to be metallic (figure 10(b)), but application of $U = 4$ eV opens a Mott–Hubbard (positive charge-transfer) d–d gap (figure 10(c)), agreeing with experimental evidence [25, 26]. Bader critical point analysis reveals Pt–Pt bonding interactions in both PtO and Pt_3O_4, consistent with previous findings by Seriani *et al* [29]. If metallic conductivity were driven solely by such Pt–Pt bonding, one

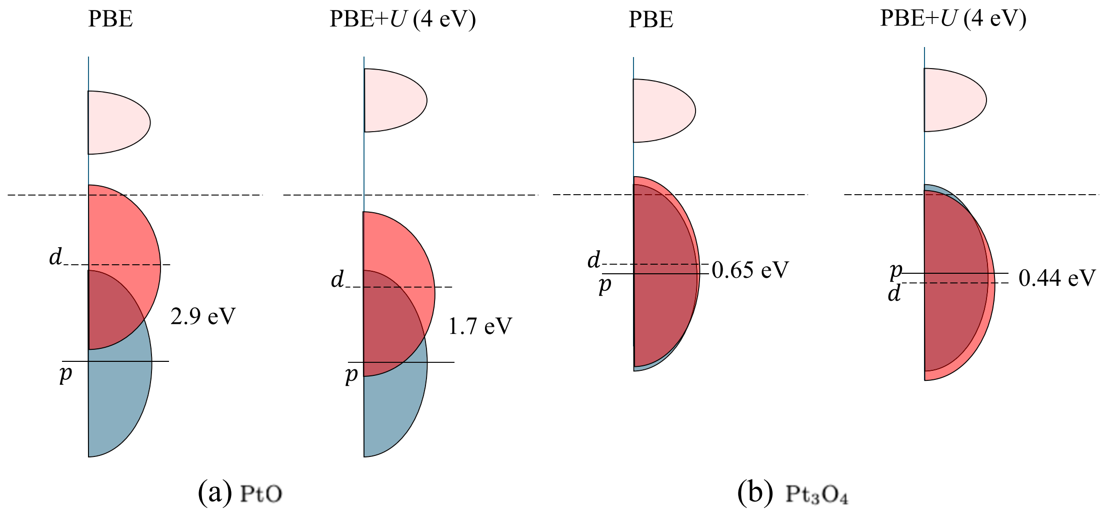

Figure 11. A schematic illustration of the relative electronic energy levels of Pt 5d-orbitals and O 2p-orbitals for (a) PtO and (b) Pt_3O_4, highlighting a positive charge-transfer phase in PtO and a mixed-valence state in Pt_3O_4. The dashed line indicates the Fermi energy level.

would expect both Pt_3O_4 and PtO to be metallic. However, PtO becomes semiconducting under moderate U, whereas Pt_3O_4 remains metallic. This difference underscores the critical role of Pt–O orbital interactions in maintaining metallic conductivity in Pt_3O_4.

Finally, we evaluated the relative electronic energy levels of PtO and Pt_3O_4 (figure 11). In PtO, Pt 5d states cross the Fermi level at $U = 0$, but are pushed down with increasing U, opening a positive charge-transfer (Mott–Hubbard) gap while the O 2p states lie well below the Fermi level, figure 11(a). In Pt_3O_4, Pt 5d states are lower in energy due to the higher oxidation state, which improves hybridization with the O 2p orbitals and reduces the charge-transfer gap, figure 11(b). This leads to a small positive charge-transfer energy and potential mixed-valence behavior, analogous to Fe_3O_4 [71]. Even though Pt_3O_4 shows signatures of weak charge disproportionation, indicating a mixed-valence phase, the Pt ions do not localize into distinct Pt^{II} and Pt^{III} sites as observed in Fe_3O_4 [72–75]. Strong Pt–O covalency in Pt_3O_4 prevents full d-orbital localization with the application of U which, when coupled with small charge transfer conduction of Pt–O orbital interactions, preserves the metallic character even under strong U, in stark contrast to PtO.

4. Summary and conclusions

We have conducted a comprehensive first-principles study of Pt_3O_4, a platinum oxide phase relevant to electrochemical energy conversion systems, using multiple levels of theory. Our investigation included GGA PBE, meta-GGA (r^2SCAN), SOC, and Hubbard U corrections to evaluate the structural and electronic properties of Pt_3O_4. Our results show that large U values (e.g. 8 eV) destabilize the experimentally observed cubic symmetry, driving the system toward a distorted structure, and are therefore unsuitable for Pt oxides. Bader charge analysis reveals that even minor structural distortions can induce limited charge disproportionation; though not of sufficient magnitude to confirm distinct Pt^{II}/Pt^{III} or Pt^{II}/Pt^{IV} states.

Importantly, Pt_3O_4 exhibits metallic behavior consistently across all functionals, regardless of the inclusion of U or SOC. This conductivity arises from a combination of delocalized Pt–Pt states and hybridized Pt–O–Pt interactions at the Fermi level. COHP analysis shows that while the contributions of Pt–Pt states progressively diminish at high values of U (e.g. 8 eV), Pt–O–Pt states remain robust, maintaining metallic nature. The persistence of these O 2p-derived pathways reflects the small charge-transfer energy in Pt_3O_4, which stabilizes mixed-valent Pt centers, as supported by Bader charge analysis. In contrast, PtO, despite its structural similarity, behaves as a positive charge-transfer insulator that develops a band gap under modest U, highlighting a key distinction in the electronic structures of these two oxides. The comparison of PtO and Pt_3O_4 underscores the critical role of Pt–O hybridization in maintaining conductivity in Pt_3O_4.

These findings clarify the origin of metallicity in Pt_3O_4 and establish its potential relevance as a conductive phase under ORR conditions in fuel cells and URFCs.

Data availability statement

All data that support the findings of this study are included within the article (and any supplementary files).

Acknowledgments

The authors acknowledge Laboratory Directed Research and Development (LDRD) Project Number 20240061DR. This research used resources provided by the Los Alamos National Laboratory Institutional Computing Program. Los Alamos National Laboratory is operated by Triad National Security, LLC, for the National Nuclear Security Administration of US Department of Energy (Contract No. 89233218CNA000001).

Author contributions

Akhil R Peeketi 0000-0002-9955-7129
Conceptualization (lead), Formal analysis (lead), Investigation (lead), Methodology (lead), Validation (lead), Visualization (lead), Writing – original draft (lead), Writing – review & editing (lead)

Lavie Rekhi 0000-0002-1039-9292
Investigation (supporting), Methodology (supporting), Writing – review & editing (supporting)

Alexander R Muñoz 0000-0002-2630-1608
Conceptualization (supporting), Formal analysis (supporting), Methodology (supporting), Writing – review & editing (equal)

Rahul Jayan 0000-0003-4073-3770
Investigation (supporting), Methodology (supporting), Writing – review & editing (supporting)

Edward F Holby 0000-0001-8419-6298
Conceptualization (supporting), Funding acquisition (supporting), Investigation (supporting), Methodology (supporting), Resources (supporting), Software (supporting), Supervision (supporting), Writing – review & editing (supporting)

Blas P Uberuaga 0000-0001-6934-6219
Conceptualization (supporting), Investigation (supporting), Methodology (supporting), Resources (supporting), Software (supporting), Supervision (supporting), Writing – review & editing (supporting)

Travis E Jones
Conceptualization (equal), Formal analysis (supporting), Funding acquisition (lead), Investigation (supporting), Methodology (lead), Project administration (lead), Resources (lead), Supervision (lead), Writing – original draft (supporting), Writing – review & editing (lead)

References

[1] Gasteiger H A, Kocha S S, Sompalli B and Wagner F T 2005 Activity benchmarks and requirements for Pt, Pt-alloy and non-Pt oxygen reduction catalysts for PEMFCs *Appl. Catal. B* **56** 9–35

[2] Wu J and Yang H 2013 Platinum-based oxygen reduction electrocatalysts *Acc. Chem. Res.* **46** 1848–57

[3] Zhang C, Shen X, Pan Y and Peng Z 2017 A review of Pt-based electrocatalysts for oxygen reduction reaction *Front. Energy* **11** 268–85

[4] Sadhasivam T, Dhanabalan K, Roh S-H, Kim T-H, Park K-W, Jung S, Kurkuri M D and Jung H-Y 2017 A comprehensive review on unitized regenerative fuel cells: crucial challenges and developments *Int. J. Hydrog. Energy* **42** 4415–33

[5] Wang Y, Wang D and Li Y 2021 A fundamental comprehension and recent progress in advanced Pt-based ORR nanocatalysts *SmartMat* **2** 56–75

[6] Brandes B A, Krishnan Y, Buchauer F L, Hansen H A and Hjelm J 2024 Unifying the ORR and OER with surface oxygen and extracting their intrinsic activities on platinum *Nat. Commun.* **15** 7336

[7] Nørskov J K, Rossmeisl J, Logadottir A, Lindqvist L, Kitchin J R, Bligaard T and Jonsson H 2004 Origin of the overpotential for oxygen reduction at a fuel-cell cathode *The J. Phys. Chem. B* **108** 17886–92

[8] Chen W, Huang J, Wei J, Zhou D, Cai J, He Z-D and Chen Y-X 2018 Origins of high onset overpotential of oxygen reduction reaction at Pt-based electrocatalysts: a mini review *Electrochem. Commun.* **96** 71–76

[9] Eckl M J, Mattausch Y, Jung C K, Kirsch S, Schmidt L, Huebner G, Mueller J E, Kibler L A and Jacob T 2022 The influence of platinum surface oxidation on the performance of a polymer electrolyte membrane fuel cell–probing changes of catalytically active surface sites on a polycrystalline platinum electrode for the oxygen reduction reaction *Electrochem. Sci. Adv.* **2** e2100049

[10] Friebel D, Miller D J, O'Grady C P, Anniyev T, Bargar J, Bergmann U, Ogasawara H, Wikfeldt K T, Pettersson L G M and Nilsson A 2011 In situ x-ray probing reveals fingerprints of surface platinum oxide *Phys. Chem. Chem. Phys.* **13** 262–6

[11] Björling A, Herrero E and Feliu J M 2011 Electrochemical oxidation of Pt(1 1 1) vicinal surfaces: Effects of surface structure and specific anion adsorption *J. Phys. Chem.* C **115** 15509–15

[12] Gómez-Marín A M and Feliu J M 2012 Pt(1 1 1) surface disorder kinetics in perchloric acid solutions and the influence of specific anion adsorption *Electrochim. Acta* **82** 558–69

[13] Fuchs T, Drnec J, Calle-Vallejo F, Stubb N, Sandbeck D J S, Ruge M, Cherevko S, Harrington D A and Magnussen O M 2020 Structure dependency of the atomic-scale mechanisms of platinum electro-oxidation and dissolution *Nat. Catal.* **3** 754–61

[14] Ruge M, Drnec J, Rahn B, Reikowski F, Harrington D A, Carlà F, Felici R, Stettner J and Magnussen O M 2017 Electrochemical oxidation of smooth and nanoscale rough Pt(1 1 1): An in situ surface x-ray scattering study *J. Electrochem. Soc.* **164** H608

[15] Wakisaka M, Asizawa S, Uchida H and Watanabe M 2010 In situ STM observation of morphological changes of the Pt(1 1 1) electrode surface during potential cycling in 10 mM HF solution *Phys. Chem. Chem. Phys.* **12** 4184–90

[16] Mom R, Frevel L, Velasco-Vélez J-J, Plodinec M, Knop-Gericke A and Schlögl R 2019 The oxidation of platinum under wet conditions observed by electrochemical x-ray photoelectron spectroscopy *J. Am. Chem. Soc.* **141** 6537–44

[17] Javed H, Knop-Gericke A and Mom R V 2022 Structural model for transient Pt oxidation during fuel cell start-up using electrochemical x-ray photoelectron spectroscopy *ACS Appl. Mater. Interfaces* **14** 36238–45

[18] Jain A *et al* 2013 Commentary: the materials project: a materials genome approach to accelerating materials innovation *APL Materials* **1** 011002

[19] Persson K A, Waldwick B, Lazic P and Ceder G 2012 Prediction of solid-aqueous equilibria: Scheme to combine first-principles calculations of solids with experimental aqueous states *Phys. Rev. B* **85** 235438

[20] Banerjee R, Chen D A, Karakalos S, Piedboeuf M-L C, Job N and Regalbuto J R 2018 Ambient oxidation of ultrasmall platinum nanoparticles on microporous carbon catalyst supports *ACS Appl. Nano Mater.* **1** 5876–84

[21] Guinel M J-F, Brodusch N, Verde-Gómez Y, Escobar-Morales B and Gauvin R 2013 Multi-walled carbon nanotubes decorated by platinum catalyst nanoparticles–examination and microanalysis using scanning and transmission electron microscopies *J. Microsc.* **252** 49–57

[22] Hejral U, Vlad A, Nolte P and Stierle A 2013 In situ oxidation study of Pt nanoparticles on MgO(0 0 1) *J. Phys. Chem.* C **117** 19955–66

[23] N M Marković and Ross P N Jr 2002 Surface science studies of model fuel cell electrocatalysts *Surf. Sci. Rep.* **45** 117–229

[24] Nie Y, Li L and Wei Z 2015 Recent advancements in Pt and Pt-free catalysts for oxygen reduction reaction *Chem. Soc. Rev.* **44** 2168–201

[25] Abe Y, Kawamura M and Sasaki K 1999 Preparation of PtO and α-PtO_2 thin films by reactive sputtering and their electrical properties *Jpn. J. Appl. Phys.* **38** 2092

[26] McBride J R, Graham G W, Peters C R and Weber W H 1991 Growth and characterization of reactively sputtered thin-film platinum oxides *J. Appl. Phys.* **69** 1596–604

[27] Zhensheng J, Chanjuan X, Qingmei Z, Feng Y, Jiazheng Z and Jinzhen X 2003 Catalytic behavior of nanoparticle α-PtO_2 for ethanol oxidation *J. Mol. Catal. A* **191** 61–66

[28] Uddin J, Peralta J E and Scuseria G E 2005 Density functional theory study of bulk platinum monoxide *Phys. Rev. B* **71** 155112

[29] Seriani N, Jin Z, Pompe W and Ciacchi L C 2007 Density functional theory study of platinum oxides: from infinite crystals to nanoscopic particles *Phys. Rev. B* **76** 155421

[30] Seriani N, Pompe W and Ciacchi L C 2006 Catalytic oxidation activity of Pt_3O_4 surfaces and thin films *The J. Phys. Chem. B* **110** 14860–9

[31] Leonov I, Yaresko A, Antonov V, Korotin M and Anisimov V 2004 Charge and orbital order in Fe_3O_4 *Phys. Rev. Lett.* **93** 146404

[32] Li J, Yu Y, Jiang S P and Liu Z-Q 2026 Electronic engineering of spinels for advanced electrocatalysis *Nanoscale Horiz.* (https://doi.org/10.1039/D5NH00539F)

[33] Wang H, Zhai T, Wu Y, Zhou T, Zhou B, Shang C and Guo Z 2023 High-valence oxides for high performance oxygen evolution electrocatalysis *Adv. Sci.* **10** 2301706

[34] Zhong X *et al* 2021 Boosting oxygen reduction activity and enhancing stability through structural transformation of layered lithium manganese oxide *Nat. Commun.* **12** 3136

[35] Yang Y, Sugino O and Ohno T 2012 Band gap of β-PtO_2 from first-principles *AIP Adv.* **2** 022172

[36] Zhou G, Li P, Ma Q, Tian Z and Liu Y 2018 Density functional theory plus hubbard U study of the segregation of Pt to the CeO_{2-x} grain boundary *Nano Lett.* **18** 1668–77

[37] Wang L, Maxisch T and Ceder G 2006 Oxidation energies of transition metal oxides within the GGA+ U framework *Phys. Rev. B* **73** 195107

[38] Lutfalla S, Shapovalov V and Bell A T 2011 Calibration of the DFT/GGA+ U method for determination of reduction energies for transition and rare earth metal oxides of Ti, V, Mo and Ce *J. Chem. Theory Comput.* **7** 2218–23

[39] Capdevila-Cortada M, Łodziana Z and López N 2016 Performance of DFT+ U approaches in the study of catalytic materials *Acs Catal.* **6** 8370–9

[40] Panda S, Bhowal S, Delin A, Eriksson O and Dasgupta I 2014 Effect of spin orbit coupling and hubbard U on the electronic structure of IrO_2 *Phys. Rev. B* **89** 155102

[41] Cococcioni M and De Gironcoli S 2005 Linear response approach to the calculation of the effective interaction parameters in the LDA+ U method *Phys. Rev. B* **71** 035105

[42] Chen J, Wu X and Selloni A 2011 Electronic structure and bonding properties of cobalt oxide in the spinel structure *Phys. Rev. B* **83** 245204

[43] Tesch R and Kowalski P M 2022 Hubbard U parameters for transition metals from first principles *Phys. Rev. B* **105** 195153

[44] Jain A, Hautier G, Ong S P, Moore C J, Fischer C C, Persson K A and Ceder G 2011 Formation enthalpies by mixing GGA and GGA+ U calculations *Phys. Rev. B* **84** 045115

[45] Selcuk S and Selloni A 2015 DFT + U study of the surface structure and stability of Co_3O_4 (110): dependence on U *J. Phys. Chem.* C **119** 9973–9

[46] Chen J and Selloni A 2012 Electronic states and magnetic structure at the Co_3O_4 (110) surface: A first-principles study *Phys. Rev. B* **85** 085306

[47] Ping Y, Galli G and Goddard W A 2015 Electronic structure of IrO_2: the role of the metal *d* orbitals *J. Phys. Chem.* C **119** 11570–7

[48] Kothakonda M, Kaplan A D, Isaacs E B, Bartel C J, Furness J W, Ning J, Wolverton C, Perdew J P and Sun J 2023 Testing the r^2SCAN density functional for the thermodynamic stability of solids with and without a van der Waals correction *ACS Mater. Au* **3** 102–11

[49] Caucci M K, Sivak J T, Almishal S S I, Rost C M, Dabo I, Maria J-P and Sinnott S B 2025 Performance of exchange-correlation approximations to density functional theory for rare-earth oxides *Comput. Mater. Sci.* **253** 113837

[50] Swathilakshmi S, Devi R and Gautam G S 2023 Performance of the r^2SCAN functional in transition metal oxides *J. Chem. Theory Comput.* **19** 4202–15

[51] Sah R K, Zdilla M J, Borguet E and Perdew J P 2024 Comparison of meta-GGAs, DFT+ U corrections and hybrid functionals for polaronic point defects in layered MnO_2, NiO_2 and $KCoO_2$ *Phys. Rev. B* **110** 184114

[52] Błoński P, Dennler S and Hafner J 2011 Strong spin–orbit effects in small Pt clusters: Geometric structure, magnetic isomers and anisotropy *J. Chem. Phys.* **134** 034107

[53] Povzner A, Volkov A and Filanovich A 2010 Electronic structure and magnetic susceptibility of nearly magnetic metals (palladium and platinum) *Phys. Solid State* **52** 2012–8

[54] Bader R F W 1990 *Atoms in Molecules: A Quantum Theory* (Clarendon)

[55] Henkelman G, Arnaldsson A and Jónsson H 2006 A fast and robust algorithm for bader decomposition of charge density *Comput. Mater. Sci.* **36** 354–60

[56] Yu M and Trinkle D R 2011 Accurate and efficient algorithm for bader charge integration *J. Chem. Phys.* **134** 064111

[57] Dronskowski R and Bloechl P E 1993 Crystal Orbital Hamilton Population (COHP): energy-resolved visualization of chemical bonding in solids based on density-functional calculations *J. Phys. Chem.* **97** 8617–24

[58] Maintz S, Deringer V L, Tchougréeff A L and Dronskowski R 2016 LOBSTER: a tool to extract chemical bonding from plane-wave based DFT *J. Comput. Chem.* **37** 1030–5

[59] Kresse G and Furthmüller J 1996 Efficient iterative schemes for *ab initio* total-energy calculations using a plane-wave basis set *Phys. Rev. B* **54** 11169

[60] Muller O and Roy R 1968 Formation and stability of the platinum and rhodium oxides at high oxygen pressures and the structures of Pt_3O_4, β-PtO_2 and RhO_2 *J. Less Common. Metals* **16** 129–46

[61] Wagman D D, Parker V B, Evans W H, Halow I, Bailey S M and Schumm R H 1969 Selected values of chemical thermodynamic properties: tables for elements 35 through 53 in the standard order of arrangement *Natl. Bureau Stand.* **270-4** 96

[62] The Materials Project 2020 Materials data on Pt_3O_4 (mp-1604, data retrieved from the Materials Project database (version v2025.09.25) (available at: https://materialsproject.org/materials/mp-1604) (20 February 2025)

[63] Isaacs E B and Wolverton C 2018 Performance of the strongly constrained and appropriately normed density functional for solid-state materials *Phys. Rev. Mater.* **2** 063801

[64] Long O Y, Gautam G S and Carter E A 2020 Evaluating optimal U for 3d transition-metal oxides within the SCAN+ U framework *Phys. Rev. Mater.* **4** 045401

[65] Kurth S, Perdew J P and Blaha P 1999 Molecular and solid-state tests of density functional approximations: LSD, GGAs and meta-GGAs *Int. J. Quantum Chem.* **75** 889–909

[66] Chase M 1998. *Nist-Janaf Thermochemical tables* 4th edn (American Institute of Physics)

[67] Matsuno J, Mizokawa T, Fujimori A, Takeda Y, Kawasaki S and Takano M 2002 Different routes to charge disproportionation in perovskite-type Fe oxides *Phys. Rev. B* **66** 193103

[68] Chen H, Freeman C L and Harding J H 2011 Charge disproportionation and Jahn-Teller distortion in $LiNiO_2$ and $NaNiO_2$: a density functional theory study *Phys. Rev. B* **84** 085108

[69] Carta A, Panda A and Ederer C 2024 Emergence of a potential charge-disproportionated insulating state in $SrCrO_3$ *Phys. Rev. Res.* **6** 023240

[70] Deringer V L, Tchougréeff A L and Dronskowski R 2011 Crystal Orbital Hamilton Population (COHP) analysis as projected from plane-wave basis sets *J. Phys. Chem. A* **115** 5461–6

[71] Sawatzky G and Green R 2016 The explicit role of anion states in high-valence metal oxides *Quantum Materials: Experiments and Theory (Modeling and Simulation)* vol 6, ed E Pavarini, E Koch, J van den Brink and G Sawatzky (Verlag des Forschungszentrum Jülich) pp 1–36 (available at: https://juser.fz-juelich.de/record/819465/files/correl16.pdf)

[72] Verwey E and de Boer J H 1936 Cation arrangement in a few oxides with crystal structures of the spinel type *Recl. Trav. Chim. Pays-Bas* **55** 531–40

[73] Verwey E 1939 Electronic conduction of magnetite (Fe_3O_4) and its transition point at low temperatures *Nature* **144** 327–8

[74] Wang Y, Lee S, Zhang L, Shang S, Chen L-Q, Derecskei-Kovacs A and Liu Z-K 2014 Quantifying charge ordering by density functional theory: Fe_3O_4 and $CaFeO_3$ *Chem. Phys. Lett.* **607** 81–84

[75] Naveas N, Pulido R, Marini C, Gargiani P, Hernandez-Montelongo J, Brito I and Manso-Silván M 2023 First-principles calculations of magnetite (Fe_3O_4) above the verwey temperature by using self-consistent DFT+ U+ V *J. Chem. Theory Comput.* **19** 8610–23